LETTER

doi:10.1038/nature14500

Galaxies at redshifts 5 to 6 with systematically low dust content and high [C II] emission

P. L. Capak[1,2], C. Carilli[3,4], G. Jones[5], C. M. Casey[6], D. Riechers[7], K. Sheth[8], C. M. Carollo[9], O. Ilbert[10], A. Karim[11], O. LeFevre[10], S. Lilly[8], N. Scoville[2], V. Smolcic[12] & L. Yan[1,2]

The rest-frame ultraviolet properties of galaxies during the first three billion years of cosmic time (redshift $z > 4$) indicate a rapid evolution in the dust obscuration of such galaxies[1–3]. This evolution implies a change in the average properties of the interstellar medium, but the measurements are systematically uncertain owing to untested assumptions[4,5] and the inability to detect heavily obscured regions of the galaxies. Previous attempts to measure the interstellar medium directly in normal galaxies at these redshifts have failed for a number of reasons[6–9], with two notable exceptions[10,11]. Here we report measurements of the forbidden C II emission (that is, [C II]) from gas, and the far-infrared emission from dust, in nine typical star-forming galaxies about one billion years after the Big Bang ($z \approx 5$–6). We find that these galaxies have thermal emission that is less than 1/12 that of similar systems about two billion years later, and enhanced [C II] emission relative to the far-infrared continuum, confirming a strong evolution in the properties of the interstellar medium in the early Universe. The gas is distributed over scales of one to eight kiloparsecs, and shows diverse dynamics within the sample. These results are consistent with early galaxies having significantly less dust than typical galaxies seen at $z < 3$ and being comparable in dust content to local low-metallicity systems[12].

We have obtained rest-frame far-infrared (FIR; 3–1,000 μm) measurements of nine 'normal' (~1–4 times average luminosity, L_*) galaxies and one low-luminosity quasar at redshifts of $z = 5$–6, about one billion years after the Big Bang. These data were taken with an early 20-antenna version of the Atacama Large Millimeter Array (ALMA) in band 7 (1,090–800 μm) continuum mode with 7.5 GHz of bandwidth, ~20 min of integration, and with the compact array yielding a resolution of ~0.6 arcsec. One of the four side bands was always centred on the 158 μm [C II] line, which is the dominant FIR cooling line for neutral gas in normal star-forming galaxies[13,14] and hence is a good indicator of galaxy dynamics and the spatial extent of the interstellar medium[14,15] (ISM). The other three spectral bands yield a measurement of the dust continuum emission at $\lambda \approx 150$ μm, which is a good indicator of the total infrared luminosity for normal FIR spectral energy distributions (SEDs; see Methods section 'Derivation of physical parameters').

The objects we studied were Lyman break galaxies (LBGs) selected from the 2 square degree Cosmic Evolution Survey (COSMOS) field[16]; these LBGs (with one object later discovered to be a low-luminosity quasar) have spectroscopically determined absorption line redshifts measured by the Deep Extragalactic Imaging Multi-Object Spectrograph (DEIMOS) on the W. M. Keck-II Observatory in Hawaii. The objects were selected to be 'characteristic' with luminosities between 1 and 4 L_* and with ultraviolet spectral slopes (β) between −1.4 and −0.7. Three objects (1, 2 and 10) also meet the selection criteria for Lyman-α (Lyα) emitters at $z \approx 5.7$. When possible, ultraviolet morphologies are measured using the Hubble Space Telescope (HST) Advanced Camera For Surveys (ACS) F814W (0.8 μm) data[17]. Stellar masses were determined by fitting SED models to existing COSMOS data and new 3–5 μm photometry from the Spitzer-SPLASH survey[18] (see Methods section 'Optical and NIR data'). Rest-frame infrared luminosities were determined by assuming the range of FIR properties measured at $z \approx 2$–5 (ref. 19) and have a systematic uncertainty of 0.3 dex due to the uncertainty in the shape of the FIR SED (see Methods section 'Derivation of physical parameters').

We detect four of nine galaxies in the dust continuum (Fig. 1, Extended Data Table 1), and a mean combination (stacking) of the data on the remaining six objects yields a continuum detection of 35 ± 13 μJy. This is less than 1/12 of that expected for systems with similar ultraviolet properties at $z < 3$ assuming the worst-case systematics in our FIR determination (see Methods section 'Robustness of upper limits on dust emission'). This can be quantified with the infrared-excess to ultraviolet-slope (IRX–β) relation[4] (Fig. 2), which relates the amount of dust absorption measured in the ultraviolet to the amount of infrared re-emission and is sensitive to both dust properties and column density. We find that the measured IRX and β for our continuum detected objects and A1689-zD1[11] are consistent with the IRX–β relation for the Small Magellanic Cloud (SMC)[20], which has lower-metallicity gas, and less thermal FIR emission[21] than typical galaxies at $z < 3$. Our undetected systems appear to have even less IRX than the SMC, but could be consistent given the large systematic uncertainties. Hence, we conclude $z \approx 6$ galaxies are significantly less dust-obscured than more-evolved systems at $z < 3$, confirming previous results[1–3,6].

The very low IRX values at $\beta \approx -1.2$ implied by our non-detections are difficult to explain in the context of the very young systems expected at $z = 5$–6 (ref. 22). The simplest explanation is the systematics in our estimates of β and total infrared luminosity (L_{IR}), which would imply relatively un-obscured systems with ~45 K dust (see Methods section 'Derivation of physical parameters'). But we cannot exclude changes in the dust geometry or rapid disruption of the molecular clouds that could lead to lower IRX vales at a given β with more-normal dust temperatures[23]. Higher signal-to-noise near-infrared photometry and shorter wavelength FIR data will ultimately be needed to understand these sources.

A corollary of this result is that ultraviolet derived star-formation rates (SFRs) at high redshift ($z > 5$) should use the SMC-like IRX–β relation or assume no dust rather than the currently assumed Meurer IRX–β relation. This will decrease the ultraviolet derived SFRs by a typical factor of ~2–4 for individual galaxies from those implied by the Meurer relation for similar values of β. The effect on the global

[1]Infrared Processing and Analysis Center (IPAC), 1200 East California Boulevard, Pasadena, California 91125, USA. [2]California Institute of Technology, 1200 East California Boulevard, Pasadena, California 91125, USA. [3]National Radio Astronomy Observatory, PO Box 0, Socorro, New Mexico 87801, USA. [4]Astrophysics Group, Cavendish Laboratory, J. J. Thomson Avenue, Cambridge CB3 0HE, UK. [5]New Mexico Institute of Mining and Technology, 801 Leroy Place, Socorro, New Mexico 87801, USA. [6]Department of Astronomy, The University of Texas at Austin, 2515 Speedway, Stop C1400, Austin, Texas 78712, USA. [7]Department of Astronomy, Cornell University, 220 Space Sciences Building, Ithaca, New York 14853, USA. [8]National Radio Astronomy Observatory, 520 Edgemont Road, Charlottesville, Virginia 22903, USA. [9]Institute for Astronomy, ETH Zurich, CH-8093 Zurich, Switzerland. [10]Aix Marseille Université, CNRS, LAM (Laboratoire d'Astrophysique de Marseille), UMR 7326, 13388 Marseille, France. [11]Argelander-Institut für Astronomie, Auf dem Hügel 71, D-53121 Bonn, Germany. [12]Physics Department, University of Zagreb, Bijenička cesta 32, 10002 Zagreb, Croatia.

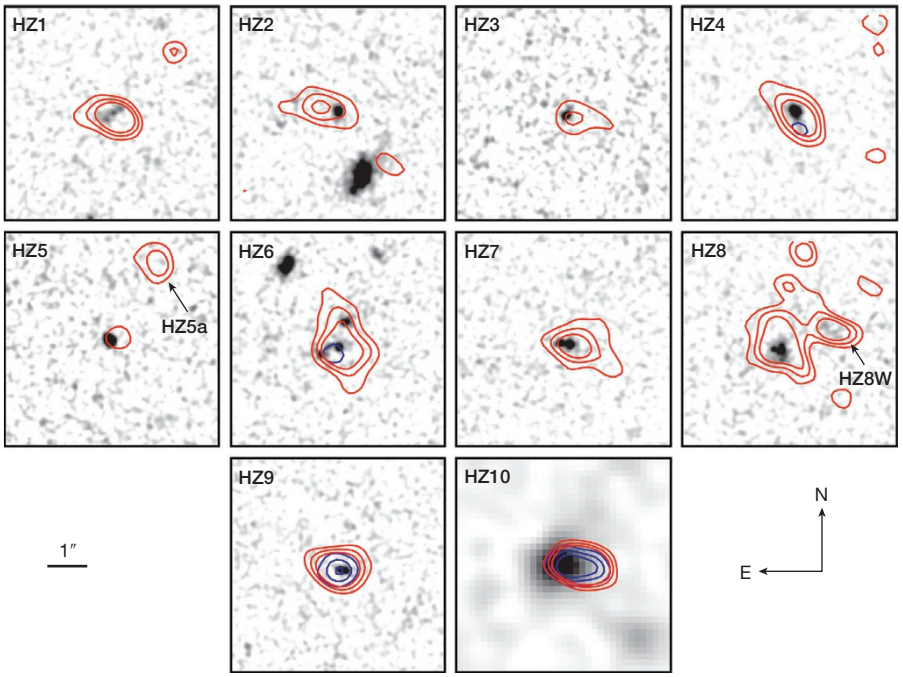

Figure 1 | Optical, [C II] and continuum maps of the sources HZ1–HZ10. The [C II] line detections (red contours) and weak ~158 μm FIR continuum detections (blue contours) are shown with the rest-frame ultraviolet images as the background. The images are 5″ × 5″ (scale bar at bottom left) and the contours are 2, 6 and 10 σ with [C II] line profiles for each source shown in Fig. 3. The background images are from HST-ACS in the F814W[17] band where the morphologies will be affected by Lyα, except for HZ10, which is Subaru z′ band. All objects are detected in [C II], showing that a large amount of gas is present in these systems, but only four are detected in continuum.

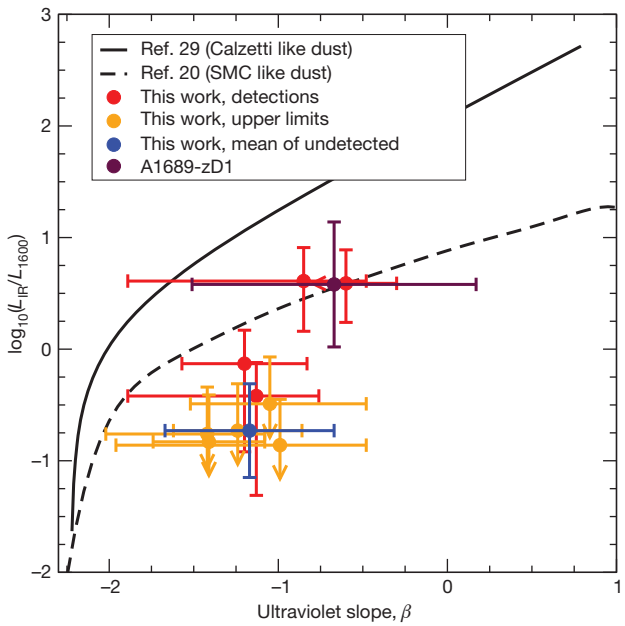

Figure 2 | IRX–β measurements of $z > 5$ objects. The deficit of infrared emission in our sample is evident in the presented infrared excess versus ultraviolet slope (IRX–β) relation when compared with models. Detections are indicated in red, upper limits in orange, the mean IRX ratio (obtained by combining undetected sources) in blue, and A1689-zD1[11] in maroon. Error bars are 1σ, and include standard measurement error and systematic uncertainty added in quadrature. The Meurer[29] relation, which assumes Calzetti-like dust and is consistent with typical galaxies at $z < 3$, is shown as a black solid line, while a model for lower-metallicity SMC-like dust model[20] is shown as a dashed line.

star-formation history is much smaller, <40%, because the majority of star-formation is in low luminosity ($<L_*$) galaxies that were already assumed to have little or no dust extinction (see Methods section 'Effects of evolving dust on the global star-formation history', Extended Data Fig. 4).

In contrast to the dust emission, we find >3σ detections of the [C II] line in all nine normal galaxies (Fig. 3). The line emission is spectrally resolved in all cases, with [C II] velocity dispersions of 63–163 km s^{-1}, and marginally resolved at our spatial resolution of ~0.5–0.9 arcsec, indicating galaxies with dynamic masses (M_{dyn}) of ~10^9–10^{11} solar masses ($M_\odot$; see Methods sections 'Reduction of ALMA data' and 'Derivation of physical parameters'). We also detect two optically faint [C II] emitters at redshifts consistent with the targeted objects. HZ5a is detected near HZ5 at a redshift consistent with the in-falling gas seen in the optical spectra of HZ5[24]. HZ8W corresponds to an optically faint companion to HZ8 and has a similar redshift. Taken together, the direct and serendipitous detections suggest ubiquitous and enhanced [C II] emission in early galaxies similar to that seen in local low-metallicity systems[12] (Fig. 4).

The [C II] enhancement in local systems is caused by a lower dust-to-gas ratio which allows the ultraviolet radiation field to penetrate a larger volume of molecular cloud[12]. Our significantly lower IRX values and enhanced [C II]/FIR ratios would suggest a similar effect is happening in high redshift galaxies. But other possible causes of the transition in obscuration properties with redshift have been suggested[25]: evolution in metal abundances that changes the intrinsic ultraviolet slope; changes in the dust properties; and differences in the dust geometry. The systems in this study were selected to have broad ultraviolet absorption features in their spectra that indicate a relatively homogeneous metal abundance of ~0.25 times the solar value. At this metallicity, the ultraviolet spectral slopes are expected to be similar to those of solar metallicity

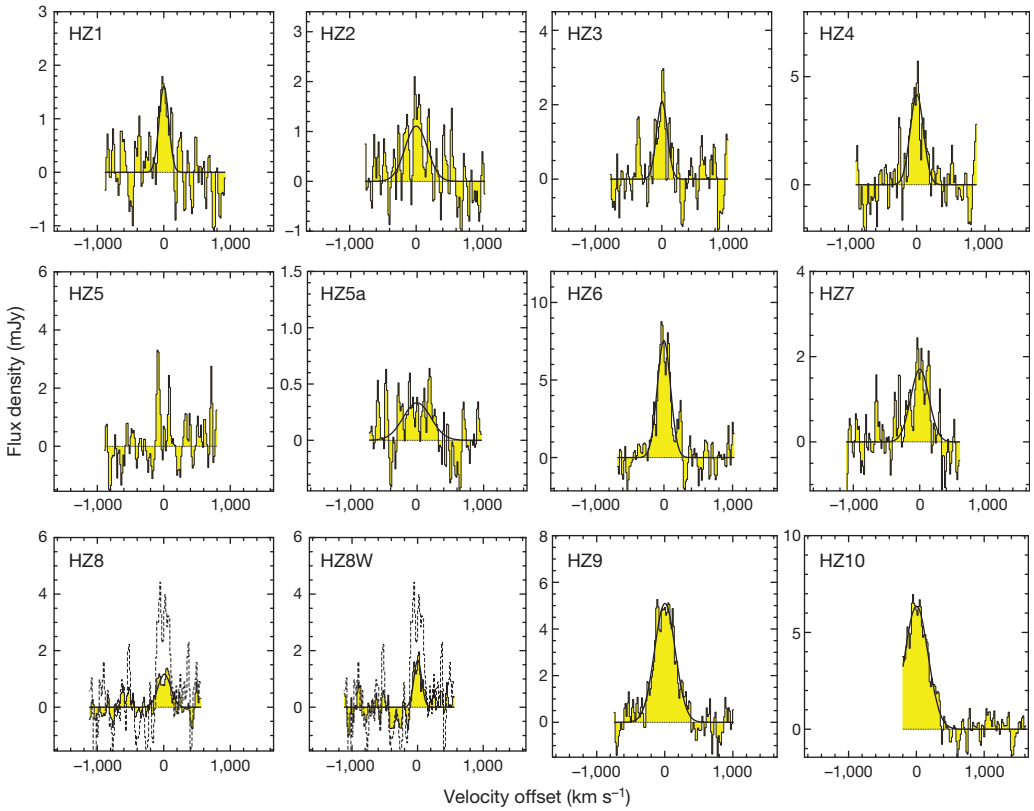

Figure 3 | [C II] line profiles for the sources. The line velocity profiles of our [C II] measurements are shown for our 10 sources and two blind detections, HZ5a and HZ8W. All sources but HZ5, a quasar, are clearly detected. For objects HZ8 and HZ8W, a dotted line showing the integrated flux over both sources is also plotted. The consistency between the integrated and individual profiles indicates they are at similar redshifts.

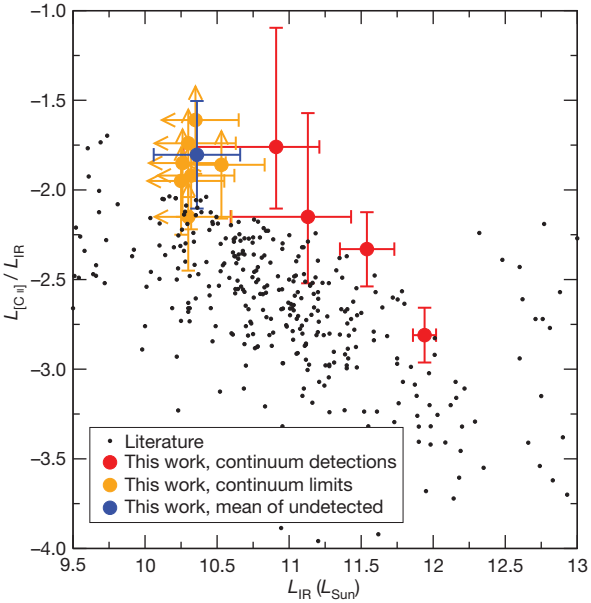

Figure 4 | $L_{[C\,II]}$ over L_{IR} ratio as a function of L_{IR}. Our sample has a clear excess of [C II] emission relative to IR emission when compared with normal lower-redshift systems ($z = 0$–3)[6,12,15,30]. Detections are indicated in red, upper limits in orange, and the mean of undetected sources is shown in blue. The high $L_{[C\,II]}/L_{IR}$ ratio we measure indicates a lower dust-to-gas ratio, more-diffuse clouds, and a more-diffuse ultraviolet radiation field than seen in normal $z \approx 0$ galaxies[12,13,15,30]. Error bars are 1σ, including standard measurement error and systematics added in quadrature.

systems[26]. Furthermore, the population from which these objects were selected has dust attenuation properties similar to those of lower-redshift objects[27]. So changes in the dust properties that would be measureable in the attenuation curve are probably not the primary factor. When compared with objects of the same stellar masses, our sample has physical properties (gas velocity dispersions, sizes, and SFRs) that imply geometries consistent with $z \approx 1$–3 galaxies that exhibit dust properties like those found in the Meurer model[28]. Changes in the average cloud geometry are therefore not obvious, but we cannot fully exclude this possibility as it would explain the observed IRX properties. So we conclude that a significant decrease in the dust-to-gas ratio is the most likely explanation for the evolution in extinction properties.

These results are seemingly at odds with previous measurements[6–9] that failed to detect [C II] emission at high redshift. Our sample contains objects with both emission and absorption of Lyα, and the [C II] emission strength is un-correlated with the Lyα properties (Extended Data Table 1), which means that the use of Lyα redshifts is not the cause. The most likely explanation for the lack of detections is observational uncertainty in the expected line flux, line width, and frequency. Even obscuration uncorrected ultraviolet SFRs will overestimate the expected FIR continuum flux, because less than 20% of the star formation is leading to FIR emission in our sample[6] (Fig. 2). This means the FIR emission of galaxies will be more difficult to detect than previously expected based on $z < 3$ scaling relations (see Methods sections 'Robustness of upper limits on dust emission' and 'Quantifying [C II] non-detections in the literature'), so longer integration times are required. That said, these data show [C II] is enhanced and readily detectable with ALMA at $z \approx 6$ if moderate integration times are used. Finally, we note that the [C II] lines are resolved in velocity space, so single channel sensitivity should not be used for

limits (see Methods section 'Quantifying [C II] non-detections in the literature').

Online Content Methods, along with any additional Extended Data display items and Source Data, are available in the online version of the paper; references unique to these sections appear only in the online paper.

Received 20 November 2014; accepted 23 April 2015.

1. Madau, P. & Dickinson, M. Cosmic star-formation history. *Annu. Rev. Astron. Astrophys.* **52,** 415–486 (2014).
2. Bouwens, R. J. *et al.* UV-continuum slopes at z ~ 4–7 from the HUDF09+ERS+ CANDELS observations: discovery of a well-defined UV color-magnitude relationship for z ≥ 4 star-forming galaxies. *Astrophys. J.* **754,** 83 (2012).
3. Finkelstein, S. L. *et al.* Candels: the evolution of galaxy rest-frame ultraviolet colors from z = 8 to 4. *Astrophys. J.* **756,** 164 (2012).
4. Reddy, N. A., Erb, D. K., Pettini, M., Steidel, C. C. & Shapley, A. E. Dust obscuration and metallicity at high redshift: new inferences from UV, Hα, and 8 μm observations of z ~ 2 star-forming galaxies. *Astrophys. J.* **712,** 1070–1091 (2010).
5. Boquien, M. *et al.* The IRX-β relation on subgalactic scales in star-forming galaxies of the Herschel Reference Survey. *Astron. Astrophys.* **539,** A145 (2012).
6. Ota, K. *et al.* ALMA observation of 158 μm [C II] line and dust continuum of a z = 7 normally star-forming galaxy in the epoch of reionization. *Astrophys. J.* **792,** 34 (2014).
7. Ouchi, M. *et al.* An intensely star-forming galaxy at z ~ 7 with low dust and metal content revealed by deep ALMA and HST observations. *Astrophys. J.* **778,** 102 (2013).
8. Maiolino, R. *et al.* The assembly of ''normal'' galaxies at z=7 probed by ALMA. Preprint at http://arXiv.org/abs/1502.06634 (2015).
9. Schaerer, D. *et al.* New constraints on dust emission and UV attenuation of z = 6.5–7.5 galaxies from millimeter observations. *Astron. Astrophys.* **574,** A19 (2015).
10. Riechers, D. A. *et al.* ALMA imaging of gas and dust in a galaxy protocluster at redshift 5.3: [C II] emission in ''typical'' galaxies and dusty starbursts ~1 billion years after the Big Bang. *Astrophys. J.* **796,** 84 (2014).
11. Watson, D. *et al.* A dusty, normal galaxy in the epoch of reionization. *Nature* **519,** 327–330 (2015).
12. Israel, F. P. & Maloney, P. R. C^+ emission from the Magellanic Clouds. II. [C II] maps of star-forming regions LMC-N 11, SMC-N 66, and several others. *Astron. Astrophys.* **531,** A19 (2011).
13. Malhotra, S. *et al.* Infrared Space Observatory measurements of [C II] line variations in galaxies. *Astrophys. J.* **491,** L27–L30 (1997).
14. Carilli, C. L. & Walter, F. Cool gas in high-redshift galaxies. *Annu. Rev. Astron. Astrophys.* **51,** 105–161 (2013).
15. Díaz-Santos, T. *et al.* Extended [C II] emission in local luminous infrared galaxies. *Astrophys. J.* **788,** L17 (2014).
16. Leauthaud, A. *et al.* Weak gravitational lensing with COSMOS: galaxy selection and shape measurements. *Astrophys. J.* **172** (Suppl.), 219–238 (2007).
17. Koekemoer, A. M. *et al.* The COSMOS survey: Hubble Space Telescope Advanced Camera for Surveys observations and data processing. *Astrophys. J.* **172** (Suppl.), 196–202 (2007).
18. Speagle, J. S., Steinhardt, C. L., Capak, P. L. & Silverman, J. D. A highly consistent framework for the evolution of the star-forming ''main sequence'' from z ~ 0–6. *Astrophys. J.*, Suppl. 214, 15–67 (2014).
19. Casey, C. M. Far-infrared spectral energy distribution fitting for galaxies near and far. *Mon. Not. R. Astron. Soc.* **425,** 3094–3103 (2012).
20. Pettini, M. *et al.* Infrared observations of nebular emission lines from galaxies at z ≈ 3. *Astrophys. J.* **508,** 539–550 (1998).
21. Gordon, K. D., Clayton, G. C., Misselt, K. A., Landolt, A. U. & Wolff, M. J. A quantitative comparison of the Small Magellanic Cloud, Large Magellanic Cloud, and Milky Way ultraviolet to near-infrared extinction curves. *Astrophys. J.* **594,** 279–293 (2003).
22. Kong, X., Charlot, S., Brinchmann, J. & Fall, S. M. Star formation history and dust content of galaxies drawn from ultraviolet surveys. *Mon. Not. R. Astron. Soc.* **349,** 769–778 (2004).
23. Charlot, S. & Fall, S. M. A simple model for the absorption of starlight by dust in galaxies. *Astrophys. J.* **539,** 718–731 (2000).
24. Capak, P. L. *et al.* A massive protocluster of galaxies at a redshift of z ~ 5.3. *Nature* **470,** 233–235 (2011).
25. Reddy, N. *et al.* GOODS-Herschel measurements of the dust attenuation of typical star-forming galaxies at high redshift: observations of ultraviolet-selected galaxies at z ~ 2. *Astrophys. J.* **744,** 154 (2012).
26. Leitherer, C., Tremonti, C. A., Heckman, T. M. & Calzetti, D. An ultraviolet spectroscopic atlas of local starbursts and star-forming galaxies: the legacy of FOS and GHRS. *Astron. J.* **141,** 37 (2011).
27. Scoville, N. *et al.* Dust attenuation in high redshift galaxies — 'diamonds in the sky'. *Astrophys. J.* **800,** 108 (2015).
28. Förster Schreiber, N. M. *et al.* The SINS survey: SINFONI integral field spectroscopy of z ~ 2 star-forming galaxies. *Astrophys. J.* **706,** 1364–1428 (2009).
29. Meurer, G. R., Heckman, T. M. & Calzetti, D. Dust absorption and the ultraviolet luminosity density at z ~ 3 as calibrated by local starburst galaxies. *Astrophys. J.* **521,** 64–80 (1999).
30. Díaz-Santos, T. *et al.* Explaining the [C II]157.7 μm deficit in luminous infrared galaxies — first results from a Herschel/PACS study of the GOALS sample. *Astrophys. J.* **774,** 68 (2013).

Acknowledgements Support for this work was provided by NASA through an award issued by JPL/Caltech. We thank the ALMA staff for facilitating the observations and aiding in the calibration and reduction process. ALMA is a partnership of ESO (representing its member states), NSF (USA) and NINS (Japan), together with NRC (Canada) and NSC and ASIAA (Taiwan), in cooperation with the Republic of Chile. The Joint ALMA Observatory is operated by ESO, AUI/NRAO and NAOJ. This work is based in part on observations made with the Spitzer Space Telescope and the W.M. Keck Observatory, along with archival data from the NASA/ESA Hubble Space Telescope, the Subaru Telescope, the Canada-France-Hawaii-Telescope and the ESO Vista telescope obtained from the NASA/IPAC Infrared Science Archive. V.S. acknowledges funding by the European Union's Seventh Framework programme under grant agreement 337595 (ERC Starting Grant, 'CoSMass').

Author Contributions P.L.C. proposed and carried out the observations, conducted the analysis in this paper, and authored the majority of the text. C.C., G.J. and K.S. carried out the reduction and direct analysis of the ALMA data. C.M.C. consulted on the spectral energy distribution fitting and interpretation of the data, and also conducted a blind test of the FIR luminosity, [C II] line luminosity, and β measurements, along with testing for sample selection effects. D.R. conducted the spectral line analysis and carried out an independent blind check of the ALMA data reduction. O.I. carried out the spectral energy distribution fitting and consulted on their interpretation. C.M.C., A.K., O.L., S.L., N.S., V.S. and L.Y. contributed to the overall interpretation of the results and various aspects of the analysis.

Author Information This paper makes use of ALMA data: ADS/JAO.ALMA#2012.1. 00523.S. ALMA. Reprints and permissions information is available at www.nature.com/reprints. The authors declare no competing financial interests. Readers are welcome to comment on the online version of the paper. Correspondence and requests for materials should be addressed to P.L.C. (capak@astro.caltech.edu).

METHODS

Cosmology. Throughout this paper we assume a simplified cosmology of $\Omega_M = 0.3$, $\Omega_V = 0.7$ and $H_o = 0.7$ when calculating physical parameters. These values approximate the 2013 Plank[31] and 9-year WMAP[32] values, and are commonly assumed in the current literature to make comparisons easier over time as the exact measured values evolve.

Reduction of ALMA data. The ALMA observatory staff, as part of standard data processing and delivery, performed initial data calibration. The calibrated visibility data were then re-analysed, and additional flagging of bad time periods in the data and bad channels was performed. The data were re-imaged using the CASA Briggs flexible weighting of the u-v visibility data with Robust = 1 to create continuum, moment zero, and channel maps. Gaussian fitting of the spectral and spatial data was performed using the CASA viewer and CASA fit tool.

The centroid frequency of these models was compared to the rest frequency of [C II] to measure the redshift, which was compared to the previously determined redshifts from optical spectroscopy. Since these measures were identical, within our precision, the reference frequency of each cube was set to the centroid frequency, allowing the FWHM of the Gaussian to be read in km s^{-1} and the line flux in Jy km s^{-1}. The [C II] line contribution was subtracted from the measured continuum fluxes.

The measurements derived from the ALMA data are given in Extended Data Table 1 and Gaussian fits done with CASA to the image components are given in Extended Data Tables 2 and 4 for the [C II] and continuum data, respectively. The fits were not constrained by the beam size, and so they can be slightly smaller due to the data errors. The errors quoted are those produced by the CASA Gaussian fitting routine and are sensitive to the box size chosen for the fit, especially in cases of low signal to noise. Deconvolved size measurements for the [C II] lines are given in Extended Data Table 3. Only objects 3 and 5a are unresolved in [C II]. In contrast, only object 10 is resolved in the continuum measurement. The baseline configuration used will resolve out spatial scales larger than 5–7″ (29–43 kpc) but none of our sources appear to have emission on that large a scale.

Optical and NIR data. These were obtained from the COSMOS photometric redshift catalogue[33] augmented with additional data from the Spitzer-Large Area Survey with Hyper-Suprime-Cam (SPLASH)[34]. Sizes were taken from the COSMOS Hubble Space Telescope Advanced Camera for Surveys (HST-ACS) weak lensing catalogue[16] and are given in Extended Data Table 5. Object 10 falls outside the area covered by HST-ACS.

Derivation of physical parameters. Since only one FIR data point was available, total infrared (3–1,100 μm) luminosity was derived using the range of grey body models covering the full range of objects observed at $z \approx 2$–5[19]. The grey body model parameters, α the blue power-law, β the long wavelength slope, and T the black body temperature, ranged between $\alpha = 1.5$–2.5, $\beta = 1.2$–2.0 and $T = 25$–45 K. The range of allowed infrared luminosities was determined by scaling these grey bodies to the observed rest frame 158 μm flux. This range of parameters resulted in a systematic uncertainty of 0.3 dex in the derived luminosity. This relatively small error is due to the fact that 158 μm is on the flat part of the SED close to the emission peak for the range of observed physical parameters. The derived infrared luminosities are given in Extended Data Table 5.

The rest frame ultraviolet properties were determined by fitting a power-law to the rest frame 0.13–0.3 μm photometry from the COSMOS and Ultra-Vista surveys. This power-law fit was then used to estimate the ultraviolet spectral slope (β) and the luminosity at 0.16 μm, where $L_{UV} = \nu_{1,600} L\nu_{1,600}$. The power-law fits appear to be biased high by the bluest bands in several cases which may be due to the intrinsic SED flatting at short wavelengths[35,36]. To account for this possible systematic, we also fit the slope using only the rest-frame 0.15–0.3 μm photometry and include the shifts in our measurement error bars. Finally, simulations[2] of observational biases from blending and signal-to-noise indicate that an additional ±0.3 systematic error should be included. These estimates are tabulated in Extended Data Table 5.

For consistency, we re-analysed A1689-zD1[11] with the same methods used for our sample. We find $L_{IR} = (6.8 \pm 1.2) \times 10^{10} L_\odot$, $L_{UV} = (1.8 \pm 0.4) \times 10^{10} L_\odot$ and $\beta = -0.67 \pm 0.78$ assuming a lensing magnification of 9.3 versus $L_{IR} = (6.2 \pm 0.8) \times 10^{10} L_\odot$ and $L_{UV} = 1.8 \times 10^{10} L_\odot$. No value was published for β derived from the photometry, but our analysis would not have produced a consistent L_{UV} if the two analyses of β were inconsistent because L_{UV} is derived from the β fit.

Stellar masses were derived using data from the Spitzer Large Area Survey with Hyper-Suprime-Cam (SPLASH) in the same way described in previous work[33]. In brief, the COSMOS and SPLASH 0.1–5 μm photometry was fitted with Bruzual and Charlot templates[37] with a Chabrier IMF allowing for a range of emission line strengths and extinction laws. The estimated stellar masses are given in Extended Data Table 5.

Dynamical masses were estimated based on the [C II] velocity dispersion ($\sigma_{[C\,II]}$) and size estimates in Extended Data Table 3. We used the method outlined in Wang *et al.*[38] to estimate the dynamical masses. In this approximation $M_{dyn} = 1.16 \times 10^5 \, V_{cir}{}^2 \, D$, where V_{cir} is the circular velocity in km s^{-1} and D is the diameter in kpc. $V_{cir} = 1.763 \, \sigma_{[C\,II]}/\sin(i)$, and i, the disk inclination angle, is approximated by the axis ratio of the object as $i = \cos^{-1}(b/a)$.

This method yields an approximate answer but is very uncertain because of our low spatial resolution that leads to a large uncertainty in both i and the object size. The errors quoted in Extended Data Table 5 include the error in the semi-major axis and the velocity dispersion and assumes $\sin(i) = 0.45$–1. This range of $\sin(i)$ approximates the range of values from a dispersion dominated system to an edge-on disk, but could be significantly larger.

We find the dynamical masses are typically a factor of ~3 greater than the stellar masses (see Extended Data Fig. 3). This is higher than the factor of 1.2–1.7 found at $z \approx 1$–3 from similar Hα based dynamical mass estimates[28], but consistent given the very large errors in our measurements.

Robustness of upper limits on dust emission. The conclusion that the dust properties, and specifically the dust mass and dust to gas ratio, of galaxies are evolving relies on two quantities: the measured deficit of rest-frame 158 μm flux, and the models that translate this into a deficit of thermal emission. Here we quantify the robustness of this result.

If we assume a Meurer *et al.* like IRX–β relation and the mean of our grey body models, the predicted mean ALMA flux of the undetected sources is 833–7,610 μJy (given the uncertainty in β), which is $>61\sigma$ discrepant from the measured mean of 35 ± 13 μJy. Individual sources are discrepant from the Meurer *et al.* relation by >17–490σ except for objects 9 and 10 which are consistent given the large errors in β. If we assume the maximal range of the systematic error, 45 K dust, $\beta = 1.5$, $\alpha = 1.2$, the predicted mean ALMA flux is 447–4,087 μJy, which is $>32\sigma$ discrepant from the measured mean. Finally we consider an extreme model with 100 K dust, $\beta = 1.5$, $\alpha = 1.2$; we predict an ALMA flux of 78–710 μJy, which is 3σ discrepant from the measured mean. In this extreme case, objects 4, 9 and 10 are consistent with the Meurer *et al.* relation, and the remaining sources are discrepant at the >1–30σ level.

We also performed a completeness analysis following Casey *et al.*[39] and find the low dust emission is unlikely to be due to selection effects in our ultraviolet sample. However, we note the result only holds for ultraviolet selected samples. The general galaxy population may contain heavily obscured objects that may not be easily found by ultraviolet selected surveys.

Quantifying [C II] non-detections in the literature. Our sample predicts a peak [C II] line flux of ~0.2–0.7 mJy for an L_* (ref. 40) galaxy with an SFR ≈ 6.5 at $z \approx 6$–7, below the detection limit of most previous studies of $z \approx 6$–7 objects[6–9].

In addition to sensitivity, we note Lyα redshifts are systematically offset by ~400 km s^{-1} and up to 1,200 km s^{-1} from the [C II] (and systemic absorption line) redshifts[41], which is a significant fraction of the ALMA band pass.

Finally, caution must be used when interpreting the limits given in the SFR–$L_{[C\,II]}$ relation because the estimated line luminosity limits scales as the square root of the assumed line width. A 36–100 km s^{-1} FWHM channel width[6–9] is typically used for these limits, but our measured line widths in Extended Data Table 1 are significantly broader. If we use our measured line widths this would predict for [C II] a line limit 0.2–1.0 dex higher than those typically quoted, making them consistent with the SFR–$L_{[C\,II]}$ relation.

Comparison of gas and SFR properties to general redshift scaling relations. This sample is enhanced in $L_{[C\,II]}$ relative to L_{IR} compared with lower-redshift samples[6] (Fig. 4). These sources have ~1% of their luminosity emitted in the [C II], consistent with low metallicity and extended star forming objects[12,15].

This sample appears to follow the local SFR–$L_{[C\,II]}$ relation if the SFR is determined by summing the ultraviolet and FIR measurements[6] rather than using a dust corrected ultraviolet estimate (Extended Data Fig. 1). However, if an ultraviolet derived dust correction is used, the points shift ~0.5–1 dex higher.

Finally we turn to the stellar-mass–SFR or 'main-sequence' relation (Extended Data Fig. 2)[18]. We find our objects generally agree with this relation, but several objects fall below the relation. Specifically, objects HZ1, HZ2 and HZ3 are below it, but HZ1 has an unusually low dynamical to stellar mass ratio, indicating the stellar mass may be over-estimated.

Effects of evolving dust on the global star-formation history. Our results indicate the properties of dust and the amount of extinction evolve significantly between $z \approx 3$, where it is well measured, and $z \approx 5$–6, where we measure it. To estimate the effect on the global star-formation history, we adopt the luminosity functions and ultraviolet slope measurements from the series of papers by Bouwens *et al.*[2,42], which are largely supported by other work[43]. We then assume the dust correction can be described by the Meurer[29] curve at $z < 4$, the SMC[20] curve at $z \approx 5$, and the SMC curve scaled to our measured IRX at $z \approx 6$–8. The results of this analysis are shown in Extended Data Fig. 4 and result in

~30–40% less star-formation at $z \approx 6$ than previously thought. For consistency with the literature, the SFR density is shown assuming a Salpeter IMF; a factor of 0.68 needs to be applied to convert to a Chabrier IMF.

Sample size. No statistical methods were used to predetermine sample size.

Randomization. The experiments were not randomized.

Blinding. The investigators were not blinded to allocation during experiments and outcome assessment.

31. Planck Collaboration. Planck 2013 results. XVI. Cosmological parameters. *Astron. Astrophys.* **571,** A16 (2014).
32. Hinshaw, G. *et al.* Nine-year Wilkinson Microwave Anisotropy Probe (WMAP) observations: cosmological parameter results. *Astrophys. J.* **208** (Suppl.), 19 (2013).
33. Ilbert, O. *et al.* Mass assembly in quiescent and star-forming galaxies since z ≃ 4 from UltraVISTA. *Astron. Astrophys.* **556,** A55 (2013).
34. Steinhardt, C. L. *et al.* Star formation at $4 < z < 6$ from the Spitzer Large Area Survey with Hyper-Suprime-Cam (SPLASH). *Astrophys. J.* **791,** L25 (2014).
35. Leitherer, C., Li, I.-H., Calzetti, D. & Heckman, T. M. Global far-ultraviolet (912-1800 Å) properties of star-forming galaxies. *Astrophys. J.* **140** (Suppl.), 303–329 (2002).
36. Buat, V., Burgarella, D., Deharveng, J. M. & Kunth, D. Spectral energy distributions of starburst galaxies in the 900–1200 Å range. *Astron. Astrophys.* **393,** 33–42 (2002).
37. Bruzual, G. & Charlot, S. Stellar population synthesis at the resolution of 2003. *Mon. Not. R. Astron. Soc.* **344,** 1000–1028 (2003).
38. Wang, R. *et al.* Star formation and gas kinematics of quasar host galaxies at z ~ 6: new insights from ALMA. *Astrophys. J.* **773,** 44 (2013).
39. Casey, C. M. *et al.* Are dusty galaxies blue? Insights on UV attenuation from dust-selected galaxies. *Astrophys. J.* **796,** 95 (2014).
40. Bouwens, R. J. *et al.* UV luminosity functions at redshifts z ~ 4 to z ~ 10: 10,000 galaxies from HST legacy fields. *Astrophys. J.* **803,** 34 (2015).
41. Shapley, A. E., Steidel, C. C., Pettini, M. & Adelberger, K. L. Rest-frame ultraviolet spectra of z ~ 3 Lyman break galaxies. *Astrophys. J.* **588,** 65–89 (2003).
42. Bouwens, R. J. *et al.* Very blue UV-continuum slope β of low luminosity z ~ 7 galaxies from WFC3/IR: evidence for extremely low metallicities? *Astrophys. J.* **708,** L69–L73 (2010).
43. Rogers, A. B. *et al.* The colour distribution of galaxies at redshift five. *Mon. Not. R. Astron. Soc.* **440,** 3714–3725 (2014).
44. De Looze, I., Baes, M., Bendo, G. J., Cortese, L. & Fritz, J. The reliability of [C ii] as an indicator of the star formation rate. *Mon. Not. R. Astron. Soc.* **416,** 2712–2724 (2011).

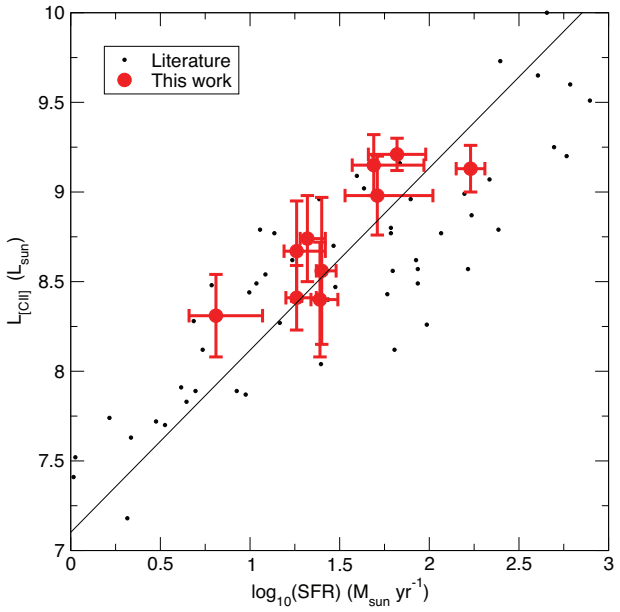

Extended Data Figure 1 | [C II] flux as a function of total star-formation rate, SFR. Our sample is consistent with the low-z SFR–$L_{[C\,II]}$ relation from the literature at $z = 0$–6 (ref. 6). The best fit to the literature points from ref. 44 is indicated with a solid line. The SFRs are derived using the UV + FIR method and a Chabrier IMF[18]. The dust-corrected ultraviolet estimates with a Meurer relation typically used at these redshifts would increase the estimated SFR by a factor of ~2–10 (0.5–1 dex), leading to over-estimates of the expected [C II] flux. The $L_{[C\,II]}$ error bars are 1σ standard measurement error, while the SFR errors are 1σ from a combination of measurement error in L_{IR} and L_{UV} converted to star formation added in quadrature.

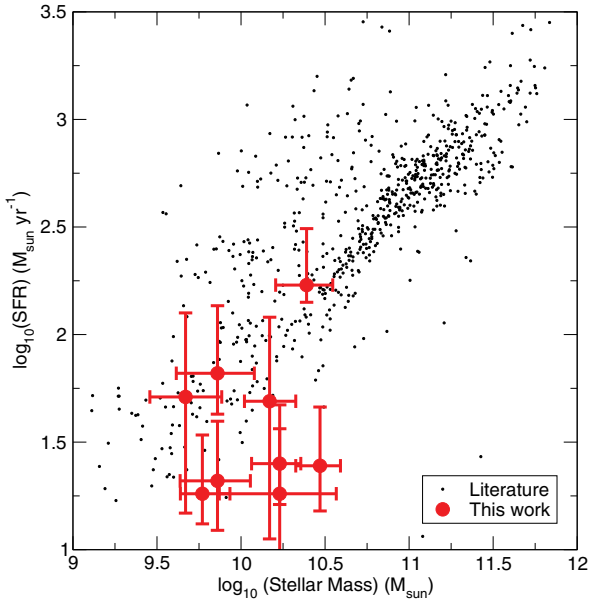

Extended Data Figure 2 | Star-formation rate as a function of stellar mass. Our objects are generally consistent with the stellar mass-SFR or 'main sequence' of star forming galaxies at $z \approx 5$–6 (ref. 18). Three objects fall below the relation, namely HZ1, HZ2 and HZ3, but the stellar mass of HZ1 may be over-estimated ('Derivation of physical parameters' in Methods). Mass errors reflect the 1σ range of masses allowed by the SED model fits including emission line strength as a free parameter. SFR errors are 1σ from a combination of measurement error in $L_{\rm IR}$, systematics in $L_{\rm IR,}$ and measurement error in $L_{\rm UV}$ converted to star formation added in quadrature.

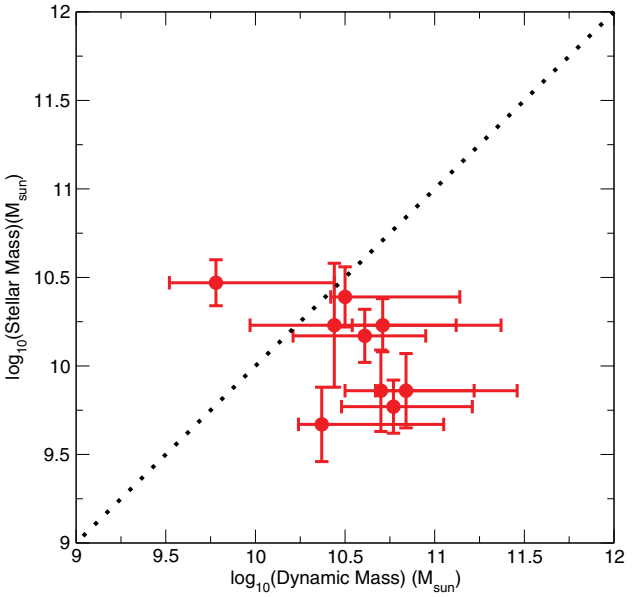

Extended Data Figure 3 | Dynamical mass compared with stellar mass. A comparison of the dynamical masses estimated from the [C II] line and stellar masses estimated from SED fitting is shown. The dotted line indicates equal stellar and dynamical masses. The average dynamic to stellar mass ratio is ~3, which is higher than, but consistent with, similar measurements at $z \approx 1$–3 (ref. 28). Errors on the dynamical masses reflect the 1σ measurement uncertainty in the size, and velocity dispersion of the sources, but the geometry is limited to $\sin(i) = 0.45$–1 ('Derivation of physical parameters' in Methods). The errors on the stellar masses reflect the 1σ range of masses allowed by the SED model fits including emission line strength as a free parameter.

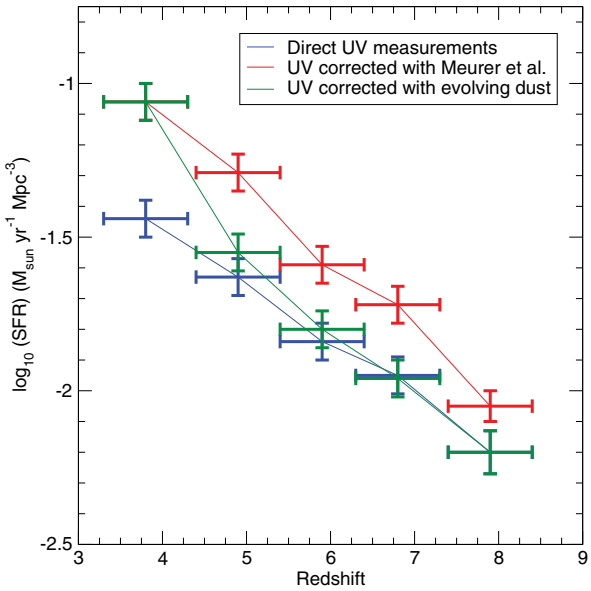

Extended Data Figure 4 | The star-formation rate history of the Universe. The global SFR history at $z > 4$ derived from UV measurements[2] is shown for three different assumptions about the dust obscuration in the general galaxy population. Blue, no correction for dust ('direct UV measurements' in key); red, a dust correction assuming the Meurer relation[29] ('UV corrected with Meurer *et al.*'); green, a correction which linearly evolves in redshift between a Meurer relation at $z \approx 4$, the SMC-like relation at $z \approx 5$, and our measured value at $z \approx 6$ ('UV corrected with evolving dust'). Note the evolving dust correction leads to a downward revision by 30–40% at $z \approx 6$. Redshift error bars reflect the binning of the data, errors in the SFR density reflect the 1σ measurement error in the ultraviolet luminosity density.

Extended Data Table 1 | Measured source properties

ID	RA	DEC	Redshift (UV) ‖	Selection†	Redshift ([CII])¶	Continuum Flux (μJy)	Line Flux (Jy km/s)	σ [CII] (km/s)‡
HZ1	149.971869	2.118175	5.690	LAE/I-LBG	5.6885(2)	<30	0.29±0.04	72±11
HZ2	150.517074	1.928902	5.670	LAE/I-LBG	5.6697(6)	<29	0.42±0.07	134±25
HZ3	150.039297	2.337183	5.546	I-LBG	5.5416(2)	<51	0.56±0.07	91±12
HZ4	149.618835	2.051873	5.540	BBG	5.5440(2)	202±47	1.14±11	108±11
HZ5§	150.214993	2.582653	5.310	V-LBG	No data	<32	<0.02	No data
HZ5a	150.214667	2.583136	No Data	[CII]	5.3089(1)	<32	0.18±0.02	20±3
HZ6*	150.08960	2.586411	5.290	V-LBG	5.2928(1)	129±36	1.80±0.13	95±7
HZ7	149.876986	2.134113	5.250	BBG	5.2532(4)	<36	0.71±0.07	162±18
HZ8	150.016896	2.626614	5.148	R-LBG	5.1533(2)	<30	0.34±0.03	107±9
HZ8W	150.016546	2.626731	No Data	[CII]	5.1532(1)	<30	0.27±0.03	63±7
HZ9	149.965406	2.378379	5.548	R-LBG	5.5410(1)	516±42	1.95±0.07	152±6
HZ10	150.247098	1.555426	5.659	LAE/I-LBG	5.6566(2)	1261±44	1.57±0.09	127±8

RA, right ascension; DEC, declination.

* This source is the same object reported as LBG-1 in ref. 25.

† LAE, Narrow band selected Lyα emitter; I-LBG, I band dropout Lyman-break galaxy; R-LBG, R band dropout Lyman-break galaxy; V-LBG, V band dropout Lyman-break galaxy; BBG, Balmer break galaxy, selected with photo-z and 4.5 μm flux; [C II], [C II] detection in these data.

‡ Velocity dispersion, FWHM $= 2.35\sigma$.

§ Chandra detected quasar, shows broad lines in spectra.

‖ Redshift error is $\pm 4 \times 10^{-3}$

¶ The numbers in parentheses indicate the errors in the final digits of the redshifts.

Extended Data Table 2 | Gaussian fits to ALMA [C II] moment zero images

ID	Beam Major Axis (“)	Beam Minor Axis (“)	Beam PA (Degrees)	Source Major Axis (“)*	Source Minor Axis (“)*	Source PA (Degrees)
HZ1	0.82	0.51	64.2	0.93±0.08	0.57±0.03	69.7±4.2
HZ2	0.91	0.5	64.9	1.46±0.37	0.69±0.08	79.3±5.6
HZ3	0.87	0.4	63.0	1.02±0.26	0.59±0.1	94±12
HZ4	0.90	0.48	59.7	1.22±0.15	0.61±0.05	43.1±4
HZ5	0.61	0.49	65.1	No Data	No Data	No Data
HZ5a	0.61	0.49	65.1	0.93±0.16	0.58±0.07	120±10
HZ6	0.68	0.48	65.2	1.07±0.14	0.83±0.09	48±17
HZ7	0.71	0.49	76.8	1.19±0.22	0.65±0.08	72.9±7.9
HZ8	0.71	0.49	61.5	1.41±0.21	1.01±0.13	35±16
HZ8W	0.71	0.49	61.5	1.05±0.13	0.55±0.04	75.3±4.2
HZ9	0.66	0.53	75.8	0.94±0.07	0.66±0.04	76.2±6.1
HZ10	0.69	0.51	60.5	1.04±0.06	0.60±0.02	78.7±2.8

PA, position angle.
* Measured source sizes, not de-convolved.

Extended Data Table 3 | De-convolved sizes of [C II] moment zero images.

ID	Major Axis (“)	Minor Axis (“)	PA (Degrees)	Major Axis (kpc)	Minor Axis (kpc)
HZ1	0.45±0.24	0.19±0.1	84±59	2.6±1.4	1.1±0.6
HZ2	1.17±0.38	0.41±0.38	86±21	6.9±2.2	2.4±2.2
HZ3	<1.02	<0.59	±180	<6.1	<3.5
HZ4	0.87±0.24	0.24±0.16	29±18	5.2±1.4	1.4±1.0
HZ5a	<0.96	<0.33	±180	<5.8	<2.0
HZ6	0.85±0.21	0.65±0.20	35±60	5.2±1.3	4.0±1.22
HZ7	0.96±0.30	0.42±0.17	72±23	5.9±1.8	2.6±1.0
HZ8	1.24±0.28	0.84±0.23	28±48	7.7±1.7	5.2±1.4
HZ8W	0.79±0.19	0.19±0.14	81±12	4.9±1.2	1.2±0.9
HZ9	0.66±0.09	0.39±0.07	76±14	3.9±0.5	2.3±0.4
HZ10	0.80±0.09	0.28±0.08	85.3±5.9	4.7±0.5	1.7±0.5

Extended Data Table 4 | Gaussian fits to ALMA continuum images*

ID	Beam Major Axis (“)	Beam Minor Axis (“)	Beam PA (Degrees)	Source Major Axis (“)	Source Minor Axis (“)	Source PA (Degrees)
HZ4	0.87	0.48	59.2	0.82±0.07	0.44±0.02	56.4±2.9
HZ6	0.71	0.50	65.5	0.72±0.06	0.45±0.02	73.9±4.2
HZ9	0.63	0.51	76.6	0.72±0.06	0.56±0.04	93±11
HZ10	0.66	0.49	61.2	1.16±0.11	0.59±0.03	83.2±3.1

* Only HZ10 is resolved in the continuum with a de-convolved size of major axis = 0.98 ± 0.13”, minor axis = 0.27 ± 0.12”, PA = 87.5 ± 5.5.

Extended Data Table 5 | Derived physical properties

ID	L_{sun} UV*	L_{sun} IR†,‡	SFR (M_{sun} yr^{-1})	L_{sun} [CII]	Beta§	UV $r^{1/2}$ (kpc)	Stellar Mass (M_{sun})	Dynamical Mass (M_{sun})
HZ1	11.15±0.05	<10.32	24^{+6}_{-3}	8.40±0.32	-1.41±0.13	1.53	10.47±0.13	$9.8^{+1.6}_{-0.8}$
HZ2	11.16±0.03	<10.3	25^{+5}_{-2}	8.56±0.41	$-0.99^{+0.41}_{-0.92}$	0.59	10.23±0.15	$10.7^{+1.6}_{-1.0}$
HZ3	11.02±0.07	<10.53	18^{+8}_{-3}	8.67±0.28	-1.05±0.5	0.66	10.23±0.35	$<10.4^{+1.6}$
HZ4	11.26±0.05	11.13±0.54	51^{+54}_{-18}	8.98±0.22	-1.20±0.36	0.72	9.67±0.21	$10.4^{+1.6}_{-1.1}$
HZ5#	11.46±0.02	<10.3	<3	<7.2	$-0.77^{+0.21}_{-0.47}$	0.37	No data	No data
HZ5a	<10.3	<10.3	<3	8.15±0.27	No data	No data	No data	$<9.0^{+1.8}$
HZ6	11.33±0.03	10.91±0.64	49^{+44}_{-12}	9.15±0.17	$-1.13^{+0.22}_{-0.71}$	3.36	10.17±0.15	$10.6^{+1.6}_{-0.8}$
HZ7	11.08±0.04	<10.35	21^{+5}_{-2}	8.74±0.24	-1.24±0.24	0.98	9.86±0.21	$10.8^{+1.5}_{-1.0}$
HZ8	11.02±0.06‖	<10.26	18^{+5}_{-2}	8.41±0.18	$-1.42^{+0.15}_{-0.52}$	1.24	9.77±0.15	$10.8^{+1.3}_{-0.9}$
HZ8W	10.57±0.15‖	<10.26	6^{+5}_{-2}	8.31±0.23	No data	1.49	No data	$9.9^{+1.6}_{-1.2}$
HZ9	10.93±0.05	11.54±0.19	67^{+30}_{-20}	9.21±0.09	$-0.85^{+0.22}_{-0.95}$**	0.95	9.86±0.23	$10.7^{+1.3}_{-1.1}$
HZ10	11.35±0.06	11.94±0.08	169^{+32}_{-27}	9.13±0.13	<-0.6¶	No data	10.39±0.17	$10.5^{+1.4}_{-1.2}$

* Monochromatic measured luminosity at rest frame 1,600 Å with no correction for obscuration. $M_{1600} = -2.5L_{UV} + 5.814$.
† ±0.3 systematic uncertainty in addition to quoted statistical errors.
‡ 3–1,100 μm integrated luminosity.
§ Systematic error is an additional ±0.3 dex based on simulations.
‖ The total ultraviolet luminosity for both components was measured as 11.15 ± 0.04 and split between the two components based on the ratio of their observed z′ magnitudes.
¶ Based on the 5σ non-detection in H band.
# Known X-ray detected quasar.
** The low SNR H band point is a significant outlier, error reflects range with that point included and rejected.